IET Research Journals

Manuscript for IET Image Processing

Journals
The Institution of Engineering and Technology

ISSN 1751-8644
doi: 0000000000
www.ietdl.org

Sparse representation for restoring images by exploiting topological structure of graph of patches

Yaxian Gao [1], *Zhaoyuan Cai* [2], *Xianghua Xie* [3], *Jingjing Deng* [4], *Zengfa Dou* [1] *Xiaoke Ma* [2,*]

[1] *School of Information Engineering,Xian University, Shaanxi, China*
[2] *School of Computer Science and Technology, Xidian University, Xi'an, Shaanxi, China*
[3] *Department of Computer Science, Swansea University, Swansea, United Kingdom*
[4] *Department of Computer Science, Durham University, Durham, United Kingdom*
* *E-mail: xkma@xidian.edu.cn*

Abstract: Image restoration poses a significant challenge, aiming to accurately recover damaged images by delving into their inherent characteristics. Various models and algorithms have been explored by researchers to address different types of image distortions, including sparse representation, grouped sparse representation, and low-rank self-representation. The grouped sparse representation algorithm leverages the prior knowledge of non-local self-similarity and imposes sparsity constraints to maintain texture information within images. To further exploit the intrinsic properties of images, this study proposes a novel low-rank representation-guided grouped sparse representation image restoration algorithm. This algorithm integrates self-representation models and trace optimization techniques to effectively preserve the original image structure, thereby enhancing image restoration performance while retaining the original texture and structural information. We evaluate the proposed method on image denoising and deblocking tasks across several datasets, demonstrating promising results.

1 Introduction

Image restoration serves as a fundamental task in image processing, aiming to reconstruct or recover the original image from degraded or corrupted signals [1]. This field has garnered extensive research attention and can generally be formulated as follows:

$$\mathbf{Y} = \mathbf{H}\mathbf{X} + \mathbf{E} \tag{1}$$

Here, $\mathbf{X}$, $\mathbf{Y}$, and $\mathbf{E}$ represent the original, degraded, and noise components of the image, respectively, while $\mathbf{H}$ denotes the degradation matrix. The restoration problem represented by Eq. (1) can vary significantly depending on the degradation matrix $\mathbf{H}$. For instance, an identity matrix for $\mathbf{H}$ corresponds to image denoising [2], a diagonal masking corresponds to image inpainting [3], and a blurring operator corresponds to image deblurring [4].

Image priors play a crucial role in image restoration, including total variation (TV) [5–7], sparsity [2, 8], low-rank [9–11], and deep image prior [12–20]. Particularly, sparsity prior is considered remarkable for natural images [2, 8, 21–24]. Current algorithms, based on strategies for manipulating sparsity prior, are roughly divided into two classes: patch-based [2, 25, 26] and group-based approaches [8, 22, 27–29].

Patch-based image restoration has received considerable attention over the past decades [2, 30]. These algorithms aim to identify low-dimensional representations (patch codes) under the assumption that each patch can be modeled with a linear combination of learned basis elements, known as a dictionary [2]. Dictionary strategies typically fall into two categories: analytic and learning-based. Analytic approaches include discrete cosine transform (DCT), wavelet, and curvelet [31]. Compared to traditional analytic methods, dictionaries learned from images are more adaptive and accurate since they comprehensively depict the local structure of images. For instance, the widely-used dictionary learning method K-SVD [30] exhibits strong adaptability and has been successfully applied to tasks like image denoising [2, 30]. Furthermore, by imposing sparse constraints on patch representations, patch-based sparse representation (PSR) achieves excellent performance for image restoration, where each patch is represented with a linear combination of a few atoms from the learned dictionary.

However, patch-based methods have been criticized for independently learning dictionaries and representations for each patch, leading to two significant limitations. Firstly, these methods are computationally time-consuming, hindering their application to large-scale image datasets. Secondly, they only exploit the intrinsic structure of each patch, disregarding the correlation among various patches, namely non-local self-similarity (NSS). To address these issues, group-based approaches, such as group sparse representation (GSR) [27, 28, 32], learn sparse coding and dictionaries from groups of similar patches, where strong correlations among them can be captured. In recent years, with the continuous development of deep neural networks (DNN), many image restoration methods based on DNN have emerged. [33] proposes a retractable transformer architecture based on attention mechanisms, which dynamically adjusts attention across different layers to restore images details more precisely. [34] proposes sparse transformer to solve deraining problems adaptively. The model leverage multi-scale features to improve the efficiency of removing rain streaks. [35] efficiently captures long-rang dependencies and preserves fine image details, enabling effective image restoration while reducing computational complexity. The image restoration algorithm based on DNN essentially achieves implicit patch similarity computation through the combination and cascading of linear layers (especially convolutional neural networks) and nonlinear layers.

Compared to patch-based methods, GSR models [25, 26] demonstrate outstanding performance in image restoration. For example, BM3D [26] performs collaborative filtering on groups of 3D patches. Mairal et al. [32] proposed LSSC, which simultaneously sparse encodes similar patches in a certain transform domain to enforce similar coefficients. Zhang et al. [27] introduced a GSR-based model for image restoration, designing a self-adaptive dictionary for image patch groups and solving sparse coding with ℓ_0 minimization. Xu et al. [36] learned an NSS prior for patch groups based on external image databases before image denoising, achieving excellent results when the distribution of external patch groups and target image patch groups is similar. To preserve the characteristics of the target image itself, a series of models combining internal and external priors are proposed [37, 38]. To obtain more correct sparsity solutions for image restoration, Wang et al. [29] incorporated nonconvex weighted ℓ_p minimization into the GSR framework for image denoising. To avoid learning dictionaries from image patches, principal component analysis (PCA) is adopted to construct dictionaries [27, 29]. Recently, Zha et al. [39] proposed the LGSR model, utilizing low-rankness to guide dictionary learning.

However, these group sparse representation models simply group similar image patches without fully exploiting the relationships between these patches and ignoring the specificity among patches within the same group. To address these issues, we propose a graph learning-guided group sparse representation image restoration algorithm. Firstly, this algorithm characterizes the similarity relationships between image patches through graph learning and performs initial reconstruction of the image to enhance the performance of subsequent sparse representation learning. Secondly, low-rank constraints are imposed during graph learning to fully explore the sub-group structure of the same group of image patches. Finally, to ensure that the learned representation satisfies sparsity while preserving the original similarity structure between image patches, the algorithm introduces trace optimization regularization. Extensive experiments are conducted to validate the superiority of the proposed algorithm over some currently popular image restoration algorithms.

The following is a summary of this research's main contributions.

- To enhance the quality of sparse representation learning, this study utilizes a graph learning model to characterize the similarity relationships between image patches and employs this model for the initial reconstruction of the image.
- In order to fully exploit the relationships between image patches while preserving the specificity of each patch, low-rank constraints are imposed during the graph learning process to identify sub-group structures within the same group of image patches.
- To ensure that the learned representation maintains sparsity while preserving the original similarity structure between image patches, this paper introduces a structural preservation regularization term into the model, thereby further improving the interpretability of sparse representation.
- Extensive experiments on two image restoration tasks, namely image denoising and inpainting, are conducted to thoroughly validate the effectiveness and superiority of the proposed algorithm.

The remaining sections of this article is arranged as follows. Section 2 introduces the preliminaries, Section 3 elaborates the proposed algorithm for image restoration in detail, Section 4 presents the experimental results, and conclusions are drawn in Section 5.

2 Preliminaries

In this section, we will present the notations and preliminaries that are going to be used for the rest of the paper.

2.1 Notations

Let the bold upper, bold lower, and lower-case letters denote matrices, vectors, and scalars, respectively. Let $\mathbf{X} \in R^{n\times m}$ be a $n \times m$ matrix, and $\mathbf{x} \in R^d$ be a vector with d elements, respectively. $\mathbf{X}^{'}$ is the transpose of matrix $\mathbf{X}$.

The Frobenius norm of matrix $\mathbf{X}$ is defined as

$$\|\mathbf{X}\| = \sqrt{tr(\mathbf{X}^{'}\mathbf{X})} = \sqrt{tr(\mathbf{X}\mathbf{X}^{'})}, \tag{2}$$

where $tr(\mathbf{X})$ is the trace of matrix $\mathbf{X}$. ℓ_0-norm of vector $\mathbf{x}$ is defined as the number of non-zero elements in $\mathbf{x}$, i.e.,

$$\|\mathbf{x}\|_0 = \sum_i |x_i|^0. \tag{3}$$

ℓ_1-norm of vector $\mathbf{x}$ is the sum of absolute values of elements in $\mathbf{x}$, i.e.,

$$\|\mathbf{x}\|_1 = \sum_i |x_i|. \tag{4}$$

ℓ_p-norm $(0 < p < 1)$ of vector $\mathbf{x}$ is defined as

$$\|\mathbf{x}\|_p = (\sum_i |x_i|^p)^{1/p}. \tag{5}$$

$\|\mathbf{X}\|_0$, $\|\mathbf{X}\|_1$ and $\|\mathbf{X}\|_p$ denotes imposing ℓ_0-norm, ℓ_1-norm, and ℓ_p-norm on each column of matrix $\mathbf{X}$, respectively. Nuclear norm of matrix $\mathbf{X}$ is defined as

$$\|\mathbf{X}\|_* = \sum_{i=1}^{min(m,n)} |\lambda_i|, \tag{6}$$

where λ_i is the i-th singular value of matrix $\mathbf{X}$.

2.2 Image Restoration

To simplify the model, we set the degradation matrix $\mathbf{H}$ as the identity matrix. Then, given a degraded image $\mathbf{Y}$, image restoration is formulated as

$$\mathbf{Y} = \mathbf{X} + \mathbf{E}, \tag{7}$$

where $\mathbf{X}$ and $\mathbf{E}$ denote the original image and additive noise, respectively. Without loss of generality, image prior is denoted by θ and then maximum a posteriori (MAP) framework [8, 27, 40] is employed, i.e., a posteriori function of the form $\log p(\mathbf{X}|\mathbf{Y}, \theta)$ is maximized

$$\log p(\mathbf{X}|\mathbf{Y}) = \log p(\mathbf{Y}|\mathbf{X}, \theta) + \log p(\mathbf{X}|\theta). \tag{8}$$

The likelihood term is the Gaussian distribution [8]

$$p(\mathbf{Y}|\mathbf{X}, \theta) = \frac{1}{\sqrt{2\pi}\sigma_E} \exp(-\frac{1}{2\sigma_E^2}\|\mathbf{Y} - \mathbf{X}\|^2), \tag{9}$$

where σ_E^2 is the noise variance. And then Eq. (8) is equal to

$$\min_{\mathbf{X}} \frac{1}{2}\|\mathbf{Y} - \mathbf{X}\|^2 + \sigma_E^2 \Theta(\mathbf{X}), \tag{10}$$

where $\Theta(\mathbf{X})$ is regularization term derived from prior θ.

2.3 Sparse Representation

Given features $\mathbf{d}_1, \ldots, \mathbf{d}_n$, representation learning for a vector $\mathbf{x}$ aims to obtain a linear function such that

$$\mathbf{x} \approx a_1\mathbf{d}_1 + \cdots + a_n\mathbf{d}_n, \tag{11}$$

where a_i is the coefficient for feature $\mathbf{x}_i$. Eq.(11) is solved by minimizing approximation, i.e.,

$$\min \frac{1}{2}\|\mathbf{x} - \mathbf{D}\mathbf{a}\|^2, \tag{12}$$

where $D = [\mathbf{x}_1, \cdots, \mathbf{x}_n]$, and $\mathbf{a} = (a_1, \ldots, a_n)^{'}$, respectively. The sparse representation learning expects most of coefficients are 0, where Eq.(11) is formulated as

$$\min \frac{1}{2}\|\mathbf{x} - \mathbf{D}\mathbf{a}\|^2 + \alpha\|\mathbf{a}\|_0, \tag{13}$$

where α is a parameter.

Furthermore, extension for sparse representation learning is needed. When multiple objects involve, i.e., $\mathbf{X} = [\mathbf{x}_1, \ldots, \mathbf{x}_n]$, GSR

IET Research Journals, pp. 1–14

simultaneously handles n objects into an objective function, where Eq.(13) is re-written as

$$\min \frac{1}{2}\|\mathbf{X}-\mathbf{D}\mathbf{A}\|^2+\alpha\|\mathbf{A}\|_0, \tag{14}$$

where $\|\mathbf{A}\|_0$ is regularization item, denotes imposing ℓ_0-norm on each column of $\mathbf{A}$.

There are various strategies for constructing sparsity, i.e., ℓ_1-norm [41][42], and ℓ_p-norm ($0 < p < 1$), to bridge ℓ_0 and ℓ_1 [43][44]. In summary, sparse representation methods assume that image patches or pixels can be represented by a small number of basis elements (atoms). And graph-based sparse representation methods decompose the image into sparse components while considering the graph structure of the image. Graph-based Sparse Coding exploits the graph structure to encourage similarity between adjacent patches, allowing for the recovery of missing parts of the image by leveraging the underlying relationships in the graph.

3 Proposed Method

In this section, we present the proposed method in detail, encompassing the restoration model, optimization, parameter selection, and discussion on its computational complexity.

The overview of the proposed algorithm is illustrated in Fig. 1, which comprises four major components: patch grouping, sparse representation learning, low-rank self-representation, and structure preservation. Patch grouping divides sub-blocks of the original images into different classes, where patches within the same groups exhibit high similarity. The low-rank self-representation module conducts self-representation learning through original image blocks and initiates the reconstruction of the image blocks. Group sparse representation learning projects each group of image blocks into a subspace spanned by dictionary matrix columns to obtain the representation of the image block, while the structure preservation module aims to ensure that the learned sparse representation maintains the original similarity structure of the image.

3.1 Restoration Model

In the patch grouping block, like other GSR-based restoration models [27, 28, 32], a patch-matching based approach is utilized. Specifically, the degraded image $\mathbf{Y}$ is divided into patches, where the size of patches varies with downstream applications. For each reference patch, the closest m patches within window of $l \times l$ are selected as a group, where patches belonging to multiple groups are allowed. To ensure the quality of groups, the step size of selected reference patches is small, where window size is large. In general, we set step size of selection reference patches as 3 or 4, and that of windows as 25×25. By stacking pixels each reference patch is denoted as $\bar{\mathbf{y}}_i$, and the corresponding patch group is $\mathbf{Y}_i$, where each column corresponds to a patch within the group.

In the sparse representation learning block, the most intuitive strategy is to project each group of patches into a subspace, where the the low-dimensional representation of patches is obtained. Specifically, given patch group $\mathbf{Y}_i$, the low-dimensional representation of patches is learned by minimizing the approximation, which is formulated as

$$\mathcal{O}(\mathbf{Y}_i)=\frac{1}{2}\|\mathbf{Y}_i-\mathbf{D}_i\mathbf{A}_i\|^2, \tag{15}$$

where $\mathbf{D}_i$ and $\mathbf{A}_i$ denotes the dictionary and coefficient matrix of $\mathbf{Y}_i$, respectively. Sparse representation learning [30] expects the learned $\mathbf{A}_i$ is sparse, i.e., the most elements are 0, which improves computational efficiency and interpretability of solutions. By imposing ℓ_1-norm constraint to coefficient matrix $\mathbf{A}_i$, Eq.(15) is reformulated as

$$\mathcal{O}(\mathbf{Y}_i)=\frac{1}{2}\|\mathbf{Y}_i-\mathbf{D}_i\mathbf{A}_i\|^2+\beta\|\mathbf{A}_i\|_1, \tag{16}$$

where parameter β determines the relative importance of sparsity constraint. Recently, evidence [43][44] demonstrates that ℓ_p-norm overcomes limitation of ℓ_1-norm to fulfill sparsity of representation. Therefore, Eq.(16) is re-written as

$$\mathcal{O}(\mathbf{Y}_i)=\frac{1}{2}\|\mathbf{Y}_i-\mathbf{D}_i\mathbf{A}_i\|^2+\beta\|\mathbf{A}_i\|_p. \tag{17}$$

In order to achieve better image restoration effects, in addition to utilizing image sparsity, the non-local self-similarity of the image should also be considered. This chapter uses low-rank self-representation to characterize the non-local self-similarity of images, that is, an image block can be represented by a linear combination of similar image blocks, and the coefficient matrix satisfies the block diagonal structure (low rank). Based on the group sparse representation model, this chapter introduces the low-rank self-representation feature, and obtains

$$\begin{aligned} O(Y_i)=&\frac{1}{2}||Y_i-D_iA_i||^2+\beta||A_i||_p\\ &+\frac{\gamma}{2}||D_iA_i-Z_i||^2+\tau||W_i||_*\\ &s.t.\quad Z_i=Z_iW_i,\, W_i={W'}_i, \end{aligned} \tag{18}$$

where Z_i is an intermediate auxiliary variable, W_i is a self-represented sparse matrix, and $||W_i||_*$ represents the nuclear norm of W_i. Different from the method proposed in the previous chapter, low-rank self-representation learning is used here to guide the learning of dictionary matrices and sparse representations at the same time, thereby further improving the quality and interpretability of sparse representation learning.

In order to prevent over-smoothing, this paper hopes that the learned sparse representation satisfies the sparsity constraints while still maintaining the similarity structure between the original image blocks. First, we perform self-representation learning on the sparse representation A_i, and the obtained self-representation matrix is as close as possible to the self-representation of the original image block, that is, minimizing

$$O(A_i)=||A_i-A_iS_i||^2-Tr({W'}_iS_i), \tag{19}$$

where S_i is the self-representation matrix of sparse coding A_i. $Tr(\cdot)$ represents the trace of the matrix, $Tr({W'}_iS_i)$ measures the similarity between matrices W_i and S_i. The combined expressions (18) and (19) can be obtained

$$\begin{aligned} O(Y_i)=&\frac{1}{2}||Y_i-D_iA_i||^2+\beta||A_i||_p+\lambda(||A_i-A_iS_i||^2\\ &-Tr({W'}_iS_i))+\frac{\gamma}{2}||D_iA_i-Z_i||^2+\tau||W_i||_*\\ &s.t.\quad Z_i=Z_iW_i,\, W_i={W'}_i, \end{aligned} \tag{20}$$

Without loss of generality, the above prior model can be substituted into the general image restoration framework 10 to obtain

$$\begin{aligned} O(Y)=&\frac{1}{2}||Y-X||+\sum_i\{\frac{\alpha}{2}||Q_iX-D_iA_i||^2+\beta||A_i||_p\\ &+\frac{\gamma}{2}||D_iA_i-Z_i||^2+\tau||W_i||_*+\lambda(||A_i-A_iS_i||^2\\ &-Tr({W'}_iS_i))\}\\ &s.t.\quad Z_i=Z_iW_i,\, W_i={W'}_i,\, \forall i \end{aligned} \tag{21}$$

where Q_i represents the matrix operator for extracting the ith group of image blocks in image X, that is, $Q_iX=X_i$. Given the degradation image Y, the restored image X can be obtained by solving the above equation. The next section will introduce the optimization process of solving this objective function.

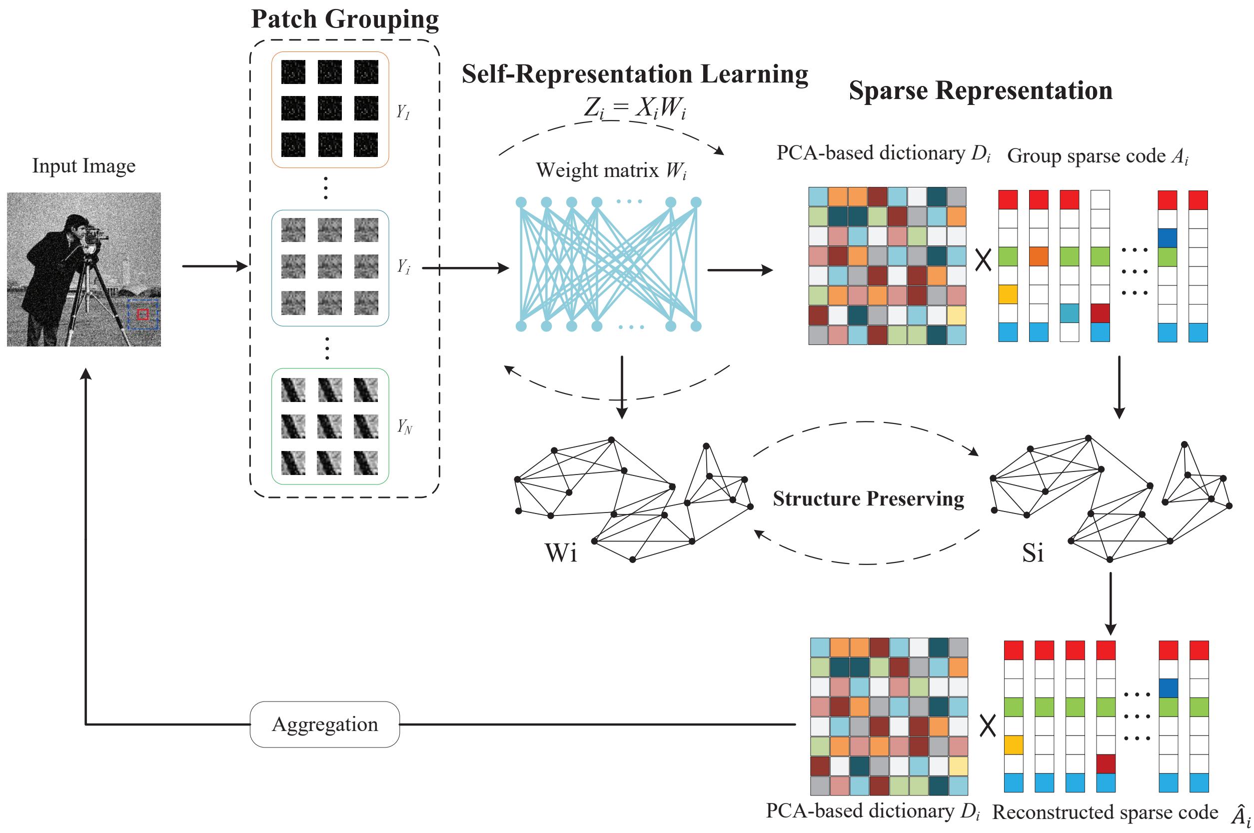

Fig. 1: Overview of the proposed image restoration algorithm, which consists of three major parts, including patch grouping, sparse representation learning and group residual learning.

3.2 Optimization

Due to the non-convex nature of the nuclear norm and l_p norm, the objective function (21) cannot directly yield an analytical solution. Therefore, this paper employs an alternating iteration strategy for optimization, wherein a single variable is optimized while keeping other variables fixed until convergence or reaching the termination condition.

1) Update Z_i and weight matrix W_i: Fixing X and A_i, and simultaneously eliminating irrelevant terms, the objective function (21) for W_i can be equivalently expressed as

$$\frac{\gamma}{2}||D_iA_i - Z_i||^2 + \tau||W_i|| * \quad \text{s.t. } Z_i = Z_iW_i, , W_i = W'i. \tag{22}$$

According to the literature [45], equation (22) can be efficiently solved by performing singular value decomposition on D_iA_i, i.e., $D_iA_i = U_i\Sigma_iV'i$, where $\Lambda_i = diag(\lambda_i)$ is a diagonal matrix containing singular values, and U_i and V_i represent the left and right singular matrices, respectively. Then, the optimal solution for Z_i in equation (22) can be expressed as

$$\hat{Z}_i = Ui1\Sigma i1V'i1, \tag{23}$$

where Σ_{i1} contains singular values greater than $\sqrt{\frac{2\tau}{\gamma}}$, while U_{i1} and V_{i1} contain the corresponding singular vectors. The optimal solution for W_i is

$$\hat{W}_i = V_{i1}V'_{i1}. \tag{24}$$

For the proof of the optimal solution of the above formula, please refer to the literature[45].

2) Update the weight matrix S_i: Eliminate terms irrelevant to S_i, and the objective function (21) can be simplified to

$$O(A_i) = ||A_i - A_iS_i||^2 - \text{Tr}(W'_iS_i). \tag{25}$$

Taking the partial derivative of S_i yields

$$A'_iA_i + A'_iA_iS_i - W_i = 0. \tag{26}$$

Setting it to 0, we obtain the update formula for S_i as

$$\hat{S}_i = (A'_iA_i)^{-1}(A'_iA_i + W_i). \tag{27}$$

3) Update group sparse representation A_i: Eliminate terms irrelevant to A_i, and the objective function (21) can be simplified to

$$\frac{\alpha}{2}||X_i - D_iA_i||^2 + \frac{\gamma}{2}||D_iA_i - Z_i||^2 + \frac{\eta}{2}||A_i - A_iS_i||^2 + \beta||A_i||_p. \tag{28}$$

By merging the first two terms, we obtain

$$\frac{1}{2}||G_i - D_iA_i||^2 + \frac{\eta}{2}||A_i - A_iS_i||^2 + \beta||A_i||_p, \tag{29}$$

where $G_i = (\alpha X_i + \gamma Z_i)/(\alpha + \gamma)$. To better adapt to the local structure of the image, this section adopts the PCA sub-dictionary strategy, i.e., learning an orthogonal dictionary through each group G_i.

After obtaining the dictionary D_i, the l_p norm makes the solution of equation (29) non-convex. Therefore, this paper utilizes the generalized soft threshold (GST) algorithm [46], an efficient iterative strategy to obtain approximate solutions. Specifically, the update rule for A_i can be expressed as

$$\hat{A}_i = \text{GST}(P_i, \mu, p, t), \tag{30}$$

where t represents the number of iterations of the GST algorithm, and the specific definitions of P_i and μ are:

$$\begin{cases} P_i = \alpha(A_i - D'_iX_i) + \gamma A_i(I - S_i - S'_i + S_iS'_i), \\ mu = \frac{\beta}{\alpha + \gamma||I - S_i||^2}. \end{cases} \tag{31}$$

4) Update the restored image X: By fixing the matrices A_i and W_i, the objective function (21) can be simplified to

$$\frac{1}{2}||Y - X||^2 + \frac{\alpha}{2}\sum_i ||Q_i X - D_i A_i||^2. \tag{32}$$

Since equation ((32)) is convex with respect to X, setting the partial derivative of (32) with respect to X to 0 yields the exact solution as

$$\hat{X} = (I + \alpha \sum_i Q'_i Q_i)^{-1}(Y + \alpha \sum_i Q'_i D_i A_i), \tag{33}$$

where $D_i A_i$ represents the reconstruction of the image patch group X_i, and Q'_i can be regarded as a matrix operator that puts the reconstructed image patch group back into the original image. In fact, $(I + \alpha \sum_i Q'_i Q_i)$ is a diagonal matrix, and its inverse can be obtained by element-wise division. Therefore, equation (33) can be regarded as superimposing the reconstructed image patches and performing a weighted average with the degraded image to obtain the restored image.

3.3 Parameter Selection

In order to obtain the best performance results, this algorithm adopts an adaptive parameter adjustment strategy to enable the proposed algorithm to adapt to various image structures. First, we update the noise variance σ_E^2 [6] using an iterative regularization strategy

$$\sigma_E^{(k)} = c0\sqrt{(\sigma_E^2 - ||Y - \hat{X}^{(k)}||^2)}, \tag{34}$$

Among them, k represents the current number of iterations, and c_0 is a positive constant.

Inspired by the maximum posterior probability framework[8], it is assumed here that the sparse encoding A_i obeys the Laplace distribution[29, 47], and the sparse residual R_i obeys the Gaussian distribution, and then the parameters can be obtained. The update strategy of β and η is

$$\beta = \frac{\sigma_E^2}{\delta_i + \epsilon}, \tag{35}$$

$$\eta = \frac{\sigma_E^2}{\delta_i^2 + \epsilon}, \tag{36}$$

Among them, δ_i represents the standard deviation of A_i, and its estimation method can be found in the document [10]. At the same time, ϵ represents a very small constant to prevent the denominator from being zero.

In addition, the parameters α and γ adopt the following update strategy:

$$\alpha = c_1 \sigma_E^2, \tag{37}$$

$$\gamma = c_2 \sigma_E^2. \tag{38}$$

Where c_1 and c_2 both represent positive constants. Formulas(37) and (38) mean that the parameters α and γ are respectively proportional to the standard deviation δ_i of the noise variance σ_E^2 .

3.4 Method Overview

To sum up, the image restoration algorithm proposed in this chapter can be realized through the above-mentioned alternating update steps and parameter adaptive adjustment mechanism. The pseudocode of the proposed algorithm is shown in Algorithm1.

3.5 Computational Complexity Analysis

In this subsection, we analyze the computational complexity of the proposed method theoretically. Concerning the spatial complexity, the proposed algorithm requires space complexity of $O(m^2 n)$. The matrices W_i and S_i for each image block group require space of $O(m^2)$. The space complexity for A_i, X_i, and Z_i for each image block group is $O(dm)$, where d represents the number of rows in A_i, X_i, and Z_i. Therefore, the total spatial complexity of the proposed algorithm is $O(m^2 n)$, where n is the number of image block groups.

Regarding the time complexity, it comprises four main components: 1) Low-rank self-representation learning, 2) Structure preservation, 3) Sparse representation learning, and 4) Image reconstruction. The time complexity for updating W_i is $O(tnm^3)$, where t is the number of iterations. The time complexity for updating S_i is $O(tnm^3)$. The time complexity for updating A_i is $O(tndm)$. The time complexity for image group reconstruction is $O(tnb^2 m)$. Hence, the total time complexity of the algorithm is $O(tnm^3)$.

Algorithm 1 The proposed algorithm for image restoration.

Input: The degraded image $\mathbf{Y}$.
Initialize $\hat{\mathbf{X}}^{(0)} = \mathbf{Y}$, $k = 0$, $\sigma_E^{(0)}$.
Set the parameters c_0, c_1, c_2 and p.
while $k <=$ Max-Iter **do**
  for each reference patch $\mathbf{x}_i$ **do** in $\hat{\mathbf{X}}^{(k)}$
    Search similar patches to construct patch group $\mathbf{X}_i$.
    Update Z_i and W_i by (23) and (24).
    Update α and γ by (37) and (38).
    Construct the dictionary $\mathbf{D}_i$ through PCA on $\mathbf{G}_i$ by (29).
    Update $\mathbf{A}_i$ by $\mathbf{A}_i = \mathbf{D}_i^{'}\mathbf{X}_i$.
    Update S_i by (27).
    Update β and η by (35) and (36).
    Update $\mathbf{A}_i$ by (30).
  end for
  Update $\hat{\mathbf{X}}^{(k)}$ by (33).
  Update $\sigma_E^{(k)}$ by (34).
  Until convergence conditions are met.
end while
Output: The restored image $\hat{\mathbf{X}}$.

4 Experimental Results

To fully validate the performance of the proposed algorithms, extensive experiments are conducted on two typical image restoration tasks: denoising and deblocking.

4.1 Experimental Setting

1) Benchmark: As the proposed algorithm follows a self-supervised learning approach, only test datasets are required to validate the performance of the proposed algorithm.

For the image denoising task, experiments are conducted on three datasets: commonly used test images (including 13 natural images, as shown in Figure **??**), the Set12 benchmark dataset [48] (consisting of 12 grayscale images), and the DND dataset [49]. DND consists of 50 high-resolution images with realistic image noise, and the DND images have been resized to 256×256. For the scene with man-made noise (the first two datasets), Gaussian noise at various levels is added to the original images to generate noisy images, which are then used for testing. For DND, there is no need to generate noisy images via manually adding Gaussian noise. Additionally, several real noisy images are also selected for experiments to thoroughly validate the algorithmâĂŹs effectiveness.

For the image deblocking task, two widely used datasets are employed: the LIVE1 dataset [50] and the Classic5 dataset [51], comprising 29 and 5 natural images, respectively. Each test image is first encoded using the MATLAB JPEG encoder at different compression quality levels Q. Subsequently, the compressed images are decoded using a standard JPEG decoder to obtain the input images for experimentation. Besides the LIVE1 and Classic5 datasets, 8 fingerprint images are also used to further validate the superiority of the proposed algorithm.

This experimental setup ensures comprehensive evaluation of the proposed algorithm's performance across various image restoration tasks.

2) Parameter Setting: For image denoising, the parameter settings of the proposed algorithm are as follows: when the noise level σ_E is ≤ 30, $30 < \sigma_E \leq 50$, and $50 < \sigma_E \leq 100$, the patch sizes are set to 7×7, 8×8, and 9×9, respectively. When $\sigma_E \leq 30$, $30 < \sigma_E \leq 40$, $40 < \sigma_E \leq 50$, $50 < \sigma_E \leq 75$, and $75 < \sigma_E \leq 100$, the number of patches per group is set to 60, 70, 80, 90, and 100, respectively. When $\sigma_E \leq 30$, $30 < \sigma_E \leq 40$, and $40 < \sigma_E \leq 100$, the parameter p is set to 0.8, 0.85, and 0.9, respectively.

For image deblocking, the patch size is set to 7×7. The number of similar patches per group is set to 60. When the compression quality Q is ≤ 10, $10 < Q \leq 20$, and $20 < Q \leq 40$, the parameter p is set to 0.9, 0.8, and 0.2, respectively.

4.2 Compared Methods

In the image denoising task, the proposed algorithm is compared with several state-of-the-art denoising methods, including BM3D [26], LSSC [32], EPLL [52], LPCA [53], NCSR [8], aGMM [54], NLN-CDR [55], SNSS [56], and LGSR [39]. Among them, algorithms such as BM3D [26], LSSC [32], EPLL [52], LPCA [53], aGMM [54], and NLN-CDR [55] utilize the prior of non-local self-similarity in images. The SNSS [57] algorithm further incorporates non-local self-similarity prior knowledge obtained through an external image database. Particularly, the NCSR [8] algorithm and the proposed algorithm in this paper are both based on sparse representation models and utilize non-local self-similarity in images for algorithmic improvement. Additionally, the proposed algorithm is compared with several deep learning-based denoising models, including TRND [58], DnCNN [48], and S2S [59]. Among these models, TRND and DnCNN are supervised learning models, while S2S is a self-supervised learning algorithm. These deep learning models serve as widely adopted baseline models.

For the image deblocking task, the proposed method is compared with various classical image deblocking methods, including BM3D [26], SA-DCT [60], PC-LRM [61], WNNM [62], ANCE [63], SSR-QC [64], COGL [65], JPG-SR [57], NSSRC [22], as well as with deep learning-based deblocking models such as AR-CNN [66], TRND [58], DnCNN [48], DCSC [67], and MDDU [68]. Among these comparison methods, AR-CNN is a commonly used deep learning baseline model for compression artifact removal, while TRND and DnCNN are general-purpose image restoration models. Lastly, DCSC and MDDU are the latest and most advanced image deblocking models.

It's worth noting that the experiments in this section were conducted with the default parameters set by the original authors for the compared methods. For deep learning models, the experiments were conducted using the pre-trained models provided by the official sources.

4.3 Image Denoising

Image denoising is the most common and fundamental task in image restoration. To validate the effectiveness of the proposed image restoration algorithm in this chapter, experiments were conducted using MATLAB's random number generator to synthesize Gaussian white noise (GWN) images for testing. Additionally, several real images were selected for denoising testing.

1) Comparison with Classical Image Denoising Methods: The proposed method and other classical denoising methods were evaluated at noise levels σ_E of 20, 30, 40, 50, 75, and 100, respectively. To quantify the effectiveness of the algorithms, two evaluation metrics were used to assess the quality of the restored images: Peak Signal-to-Noise Ratio (PSNR) and Structural Similarity Index (SSIM) [69]. Table 1 (PSNR results) and Table 2 (SSIM results) show the denoising average results of all compared methods on 13 commonly used

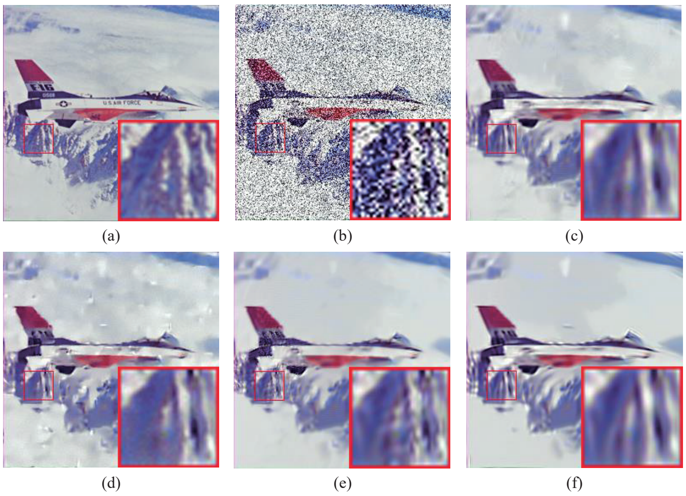

Fig. 2: Visualization of algorithms for denoising image*airplane* under $\sigma_E = 75$ noise: (a) Original image, (b) Noise image, (c) BM3D (PSNR = 23.99 dB, SSIM = 0.7488), (d) EPLL (PSNR = 23.94 dB, SSIM = 0.7168), (e) NCSR (PSNR = 23.77 dB, SSIM = 0.7551), and (f) The proposed algorithm **(PSNR = 24.25 dB, SSIM = 0.7690).**

test images, with the best results highlighted in bold. It is evident that the proposed algorithm outperforms all other compared methods overall in both PSNR and SSIM metrics. Particularly in terms of the SSIM metric, the proposed algorithm significantly outperforms other methods. The SSIM metric primarily focuses on the structural information of images, simulating human perception of image structure, and providing a more accurate assessment of image quality.

Experiments setup on real-word dataset DND follows the main approach outlined in [49]. The algorithms are applied to the space of linear raw intensity(RAW data) and RAW data with a variance stabilizing transformation(VST). After denoising, the results are compared with RAW and sRGB for evaluation respectively. Therefore, there are four separate scenarios in the experiment results, as reported in Table 3 for average PSNR and Table 4 for average SSIM respectively, where the best performance if highlighted in bold. It is obvious that performance is better in scenarios where algorithms are evaluated on the RAW space, regardless which space the algorithm is applied to. Our proposed method outperforms most other baseline methods in nearly all scenarios, except for the third scenario, where both PSNR and SSIM are slightly weaker than BM3D.

Human visual perception is the most intuitive judgment of image quality, which is crucial for evaluating image denoising algorithms. Figures 2 and 3 respectively illustrate the denoising visualization results of the proposed algorithm and other classical algorithms on images *Airplane* and *Miss* at noise level $\sigma_E = 75$. Among them, BM3D [26] adopts collaborative filtering for denoising, and it can be observed from the images that its result suffers from oversmoothing, leading to the blurring of the original texture structure. The EPLL algorithm [52] denoises based on image distribution, but the denoising result is not ideal, as there are still many artifacts remaining. The NCSR algorithm [8], like the algorithm proposed in this chapter, is based on group sparse representation model. However, it can be seen from the images that although NCSR can effectively remove noise, the image does not retain the original structure clearly, whereas the proposed algorithm in this chapter has addressed this issue as much as possible. Overall, both the SSIM results and the visualization results demonstrate the superiority of the proposed algorithm. This is attributed to the adoption of low-rank self-representation for graph learning and guiding the learning of sparse representation in this algorithm, which allows the learned sparse representation to maintain the original graph structure, thus avoiding oversmoothing to a certain extent.

2) Comparison with DNN-based Image Denoising Models: Deep Neural Networks (DNNs) have achieved significant success in both

Table 1 Average PSNR (dB) results of image denoising compared with classical methods on test image dataset

σ_E	BM3D	LSSC	EPLL	LPCA	NCSR	aGMM	NLN-CDR	SNSS	LGSR	**Ours**
20	31.87	31.98	31.44	31.31	31.85	31.78	31.21	32.09	32.15	**32.20**
30	29.86	29.88	29.88	29.40	29.72	29.69	29.02	30.11	30.21	**30.25**
40	28.25	28.41	27.95	27.48	28.29	28.22	27.84	28.68	28.65	**28.77**
50	27.26	27.26	26.82	26.25	27.16	27.10	26.73	27.62	27.62	**27.68**
75	25.31	25.16	24.82	24.09	25.08	25.02	24.82	25.65	25.67	**25.69**
100	23.92	23.69	23.46	22.61	23.60	23.63	23.58	24.33	**24.35**	24.30
Average	27.75	27.73	27.40	26.86	27.62	27.57	27.20	28.08	28.11	**28.15**

Table 2 Average SSIM results comparing image denoising with classical methods on test image dataset

σ_E	BM3D	LSSC	EPLL	LPCA	NCSR	aGMM	NLN-CDR	SNSS	LGSR	**Ours**
20	0.9014	0.9013	0.8950	0.8935	0.9004	0.8994	0.8905	0.9029	0.9056	**0.9062**
30	0.8659	0.8648	0.8549	0.8526	0.8645	0.8607	0.8357	0.8712	0.8760	**0.8764**
40	0.8303	0.8330	0.8177	0.8145	0.8346	0.8256	0.8183	0.8439	0.8456	**0.8477**
50	0.8058	0.8047	0.7836	0.7789	0.8079	0.7939	0.7879	0.8195	0.8202	**0.8231**
75	0.7440	0.7398	0.7096	0.6988	0.7518	0.7197	0.7320	0.7660	0.7658	**0.7687**
100	0.6925	0.6907	0.6477	0.6277	0.7042	0.6566	0.6964	0.7230	0.7260	**0.7262**
Average	0.8067	0.8057	0.7848	0.7777	0.8106	0.7927	0.7935	0.8211	0.8232	**0.8247**

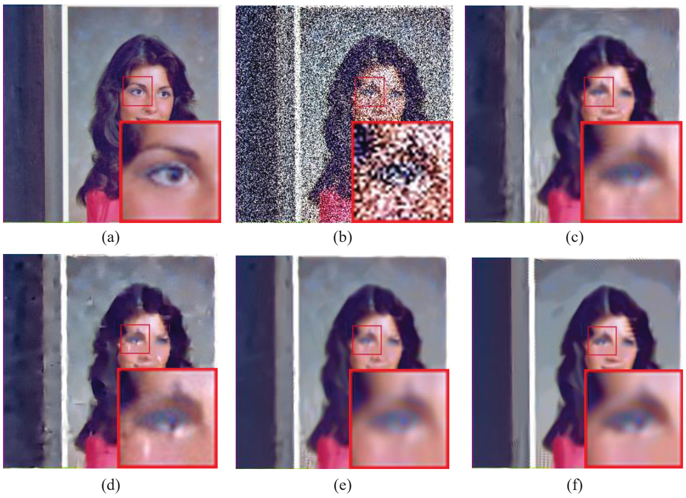

Fig. 3: Visualization of algorithms for denoising image*Miss* under $\sigma_E = 75$ noise: (a) Original image, (b) Noisy image, (c) BM3D (PSNR = 27.34 dB, SSIM = 0.7722), (d) EPLL (PSNR = 26.69 dB, SSIM = 0.7422), (e) NCSR (PSNR = 27.01 dB, SSIM = 0.7927), and (f) the proposed algorithm **(PSNR = 27.55 dB, SSIM = 0.7956).**

Table 5 Average PSNR (dB) / SSIM results comparing image denoising with DNN-based methods on the Set12 dataset

Methods	$\sigma_E = 15$	$\sigma_E = 25$	$\sigma_E = 50$	Average
TRND	32.51	30.04	26.78	29.78
	0.8970	0.8523	0.7672	0.8388
DnCNN	32.50	30.17	26.98	29.88
	0.8966	**0.8549**	0.7700	0.8405
S2S	32.07	29.94	26.12	29.38
	0.8891	0.8475	0.7382	0.8249
Ours	**32.51**	**30.17**	**27.01**	**29.90**
	0.8941	0.8538	**0.7794**	**0.8424**

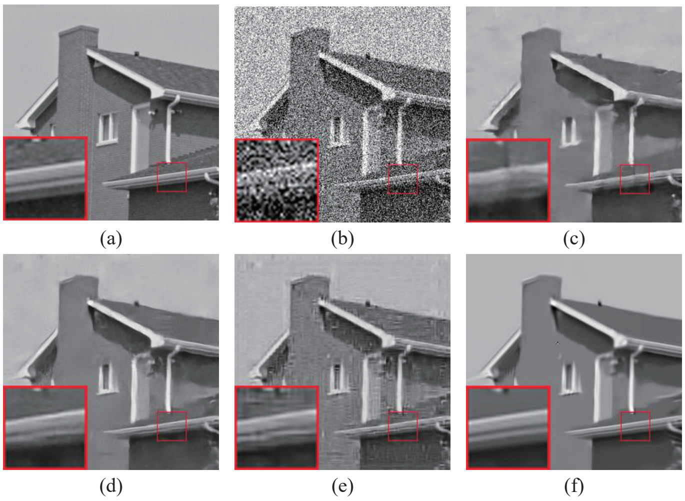

Fig. 4: Visualization of denoising results of algorithms for image *House* in the Set12 dataset under $\sigma_E = 50$ noise: (a) Original image, (b) Noisy image, (c) TRND (PSNR = 29.40 dB, SSIM = 0.8058), (d) DnCNN (PSNR = 29.74 dB, SSIM = 0.8059), (e) S2S (PSNR = 27.47 dB, SSIM = 0.7032), and (f) the proposed algorithm **(PSNR = 30.40 dB, SSIM = 0.8293).**

Fig. 5: Visualization of denoised image *Barbara* in the Set12 dataset under $\sigma_E = 50$ noise: (a) Original image, (b) Noisy image, (c) TRND (PSNR = 25.78 dB, SSIM = 0.7450), (d) DnCNN (PSNR = 25.53 dB, SSIM = 0.7361), (e) S2S (PSNR = 26.82 dB, SSIM = 0.7840), and (f) the proposed algorithm **(PSNR = 27.88 dB, SSIM = 0.8243).**

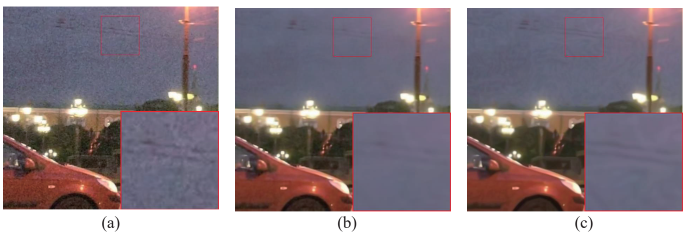

Fig. 6: Visualization of denoising for real images by various algorithms: (a) Real image, (b) S2S, and (c) the proposed algorithm.

high-level understanding and basic processing tasks of images. Therefore, this section compares the proposed algorithm with several mainstream DNN-based image denoising models, including TRND [58], DnCNN [48], and S2S [59]. The average results (PSNR and SSIM) on the Set12 dataset are shown in Table 5.

The results indicate that the proposed method outperforms some popular deep image denoising models. For better visualization, this section selects some denoising results at $\sigma_E = 50$ for visual display, as shown in Figures 4 and 5. The denoising results of TRND, DnCNN, S2S, and the proposed method are displayed in the figures. It can be observed that deep learning-based methods tend to produce artifacts or oversmoothing during denoising, while the proposed method can avoid such issues and more clearly restore the details of the image. The results indicate that although supervised deep models can be trained on large-scale datasets to fit the distribution of images as much as possible, the generalization ability of this distribution fitting is usually insufficient, resulting in unsatisfactory performance on images dissimilar to the training dataset distribution. These supervised deep models overlook the inherent structural priors of images, such as sparsity and NSS, while the proposed algorithm can effectively utilize these priors to achieve desirable results on various images. Although the S2S model and the proposed method are both self-supervised models, the deep network parameters of the S2S model lead to longer learning times compared to the proposed method.

To thoroughly validate the effectiveness of the proposed algorithm, experiments were conducted using real noisy images. As the model proposed in this chapter requires the noise variance of the images as a prior parameter, a fast noise estimation method [70] was employed to obtain the noise variance of the real images in advance. The denoising results of real noisy images are shown in Figure 6. The proposed method is compared with the S2S [59] model, which is also a self-supervised model based on deep learning. It can be clearly observed that the restoration results of S2S exhibit oversmoothing, while the proposed method preserves more image details.

(a) (b) (c) (d)

Fig. 7: Visualization of image *buildings* in the LIVE1 dataset (image size: 256×256) under compression quality $Q = 10$ deblocked by various algorithms: (a) Original image, (b) JPEG compressed image (PSNR = 23.83 dB, SSIM = 0.8232), (c) SA-DCT (PSNR = 24.66 dB, SSIM = 0.8177), and (d) the proposed algorithm **(PSNR = 25.11 dB, SSIM = 0.8311).**

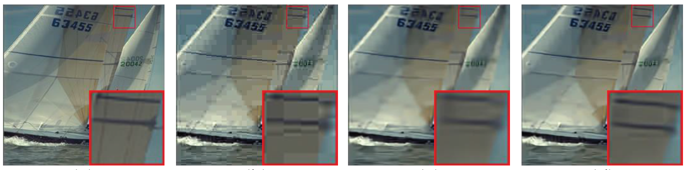

(a) (b) (c) (d)

Fig. 8: Visualization of performance of various algorithms for deblocking image *sailing3* in the LIVE1 dataset (image size: 256×256) under compression quality $Q = 10$: (a) Original image, (b) JPEG compressed image (PSNR = 28.61 dB, SSIM = 0.7561), (c) SA-DCT (PSNR = 29.62 dB, SSIM = 0.8310), and (d) the proposed algorithm **(PSNR = 29.96 dB, SSIM = 0.8457).**

4.4 Image Deblocking

To further comprehensively validate the effectiveness of the proposed algorithm, experiments were conducted on the JPEG compression artifact removal problem [60, 64, 66], which involves removing blocky artifacts from JPEG compressed images. Unlike image denoising tasks, in image deblocking, the additive noise E is quantization noise. Therefore, classic Gaussian models [60] were employed to estimate the noise standard deviation σ_E, characterizing the noise quantization process.

1) Comparison with Classical Image Deblocking Methods: To evaluate the performance of all classical deblocking methods involved in the comparison, experiments were conducted on two commonly used benchmark datasets: the LIVE1 dataset [50] and the Classic5 dataset [51]. Similar to image denoising, experiments utilized two evaluation metrics, PSNR and SSIM. The results are shown in Tables 6 and 7. It is evident that the proposed method outperforms other classical methods on the Classic5 dataset at a compression quality of $Q = 40$. Particularly, the proposed method significantly outperforms other comparison methods on low compression quality images ($Q = 10, 20, 30$) and approaches or even surpasses current state-of-the-art methods on high compression quality images ($Q = 40$).

To provide a more intuitive demonstration of the superiority of the proposed algorithm, Figure 7 and Figure 8 respectively illustrate the deblocking results of the images *buildings* and *sailing3* from the LIVE1 dataset at a compression quality of $Q = 10$. A visual comparison is made between the proposed algorithm and the popular SA-DCT image compression algorithm. From the images, it can be observed that the SA-DCT algorithm fails to fully restore the edge information of the images during the deblocking process. Portions of the edges still exhibit blocky artifacts, as highlighted by the red boxes in the figures. In contrast, the proposed algorithm is able to effectively remove the blocky artifacts while preserving the edge details of the images.

*2) Comparison with DNN-based Image Deblocking Models:*To further demonstrate the superiority of the proposed method in the image deblocking task, experiments were conducted to compare it with several deep learning-based methods, including AR-CNN [66], TRND [58], DnCNN [48], DCSC [67], and MDDU [68]. The comparison experiment was conducted on the Classic5 [51] dataset, which is a popular benchmark dataset in the field of image deblocking. Table 8 presents the average PSNR and SSIM results at different compression qualities Q.

The results indicate that the proposed method achieves better results compared to AR-CNN and TRND, while performing comparably to DnCNN, DCSC, and MDDU. It is worth noting that these supervised deep learning methods require large-scale image datasets to train the image deblocking models. It can be observed that if the training image dataset and the distribution of test images are similar or identical, then deep learning models can effectively adapt to different image structures.

Table 8 Average PSNR(db)/SSIM results comparing image deblocking with DNN-based methods on dataset Classic5

Methods	$Q = 10$	$Q = 20$	$Q = 30$	**Average**
AR-CNN	29.08	31.25	32.60	30.98
	0.7909	0.8514	0.8808	0.8410
TRND	29.29	31.48	32.79	31.19
	0.7996	0.8581	0.8841	0.8473
DnCNN	29.40	31.63	32.91	31.31
	0.8026	0.8610	0.8861	0.8499
DCSC	29.62	31.81	33.06	31.50
	0.8096	0.8641	0.8882	0.8540
MDDU	29.95	32.11	33.33	31.80
	0.8171	0.8689	0.8916	0.8592
Ours	29.43	31.65	32.88	31.32
	0.8047	0.8608	0.8855	0.8503

However, it was observed in the experimental results that deep learning methods tend to cause excessive smoothing in the restored images, especially for texture-rich images, as shown in Figure 10. To further validate this finding, experiments were conducted using eight fingerprint images collected from the NIST dataset as the test benchmark, as shown in Figure 9. The average deblocking results for the eight fingerprint images are presented in Table 9. The proposed method outperforms all other deep learning-based image deblocking methods. Visual comparison results are shown in Figure 11, where it can be observed that the proposed method reconstructs better texture details compared to other methods.

Table 9 Average PSNR(db)/SSIM results comparing image deblocking with DNN-based methods on fingerprint image dataset

Methods	$Q = 10$	$Q = 20$	$Q = 30$	**Average**
AR-CNN	30.23	33.04	34.76	32.68
	0.8859	0.9291	0.9480	0.9210
TRND	30.42	33.19	34.87	32.83
	0.8899	0.9317	0.9492	0.9236
DnCNN	30.31	33.07	34.73	32.70
	0.8894	0.9308	0.9485	0.9229
DCSC	30.52	33.13	34.78	32.81
	0.8934	0.9330	0.9497	0.9254
MDDU	30.45	32.95	34.35	32.58
	0.8961	**0.9349**	**0.9508**	0.9273
Ours	**30.81**	**33.54**	**35.20**	**33.18**
	0.8967	0.9344	0.9507	**0.9273**

4.5 Convergence

Since the proposed algorithm involves block grouping operations, non-convex optimization, and parameter updates, it is challenging to provide theoretical proof for the local convergence of the proposed algorithm. Therefore, this subsection provides experimental evidence to validate the convergence of the proposed algorithm. Five test images were selected from the test dataset, and the process of restoring these images was recorded. Figures 12(a) and 12(b) show

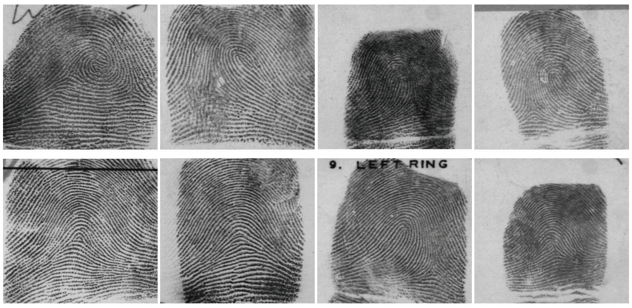

Fig. 9: Eight fingerprint test images selected from the NIST dataset.

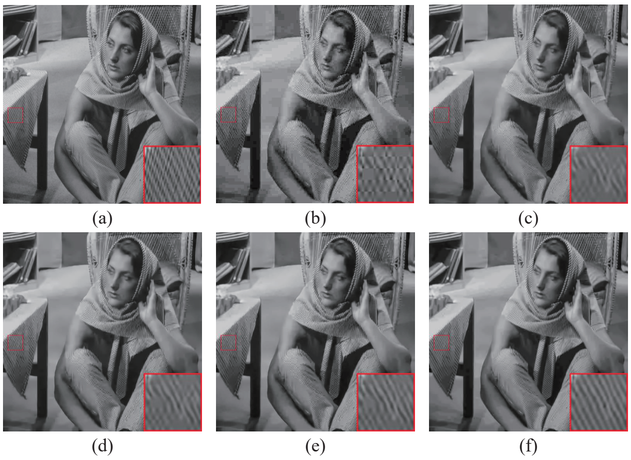

Fig. 10: Deblocking image*Barbara* in the Classic5 dataset under compression quality $Q = 10$: (a) Original image, (b) JPEG compressed image (PSNR = 25.78 dB, SSIM = 0.7621), (c) ARCNN (PSNR = 26.89 dB, SSIM = 0.7934), (d) TRND (PSNR = 27.24 dB, SSIM = 0.8104), (e) DnCNN (PSNR = 27.59 dB, SSIM = 0.8161), and (f) the proposed algorithm **(PSNR = 28.26 dB, SSIM = 0.8335).**

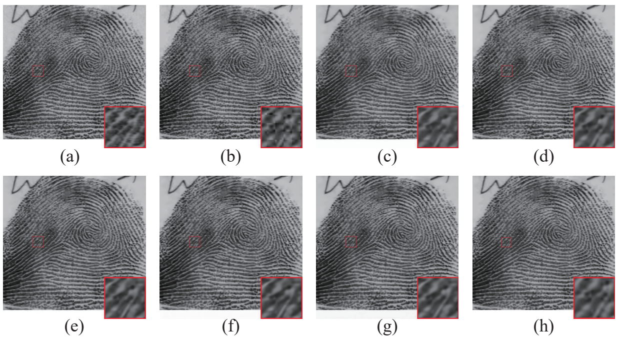

Fig. 11: Performance of algorithms for deblocking image*image 01* in the Classic5 dataset under compression quality $Q = 10$: (a) Original image, (b) JPEG compressed image (PSNR = 28.41 dB, SSIM = 0.8737), (c) ARCNN (PSNR = 29.57 dB, SSIM = 0.8969), (d) TRND (PSNR = 29.73 dB, SSIM = 0.9008), (e) DnCNN (PSNR = 29.72 dB, SSIM = 0.9019), (f) DCSC (PSNR = 29.82 dB, SSIM = 0.9045), (g) MDDU (PSNR = 29.82 dB, SSIM = 0.9081), and (h) the proposed algorithm **(PSNR = 30.13 dB, SSIM = 0.9083).**

the variation curves of PSNR values during the iterations of the image denoising with noise level $\sigma_E = 50$ and image deblocking with compression quality $Q = 10$ algorithms, respectively. It can be clearly observed that as the number of algorithm iterations increases, the PSNR curves of all restored images first monotonically increase and then gradually stabilize. Therefore, it can be proved that the proposed algorithm exhibits good convergence.

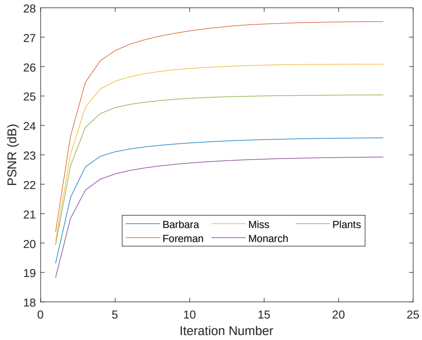

(a)

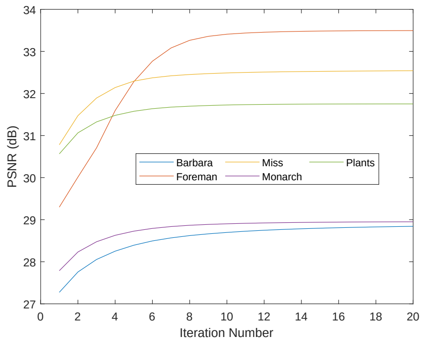

(b)

Fig. 12: Convergence of the proposed algorithm with various strategies: (a) how PSNR changes as the number of iterations increases with noise level $\sigma_E = 50$, and (b) how PSNR changes as the number of iterations increases with compression quality $Q = 10$.

4.6 *Ablation Study*

From the objective function 21, it can be seen that the proposed algorithm consists of three main modules: group sparse representation (SR), low-rank self-representation (LR), and structure preservation (SP). In order to investigate the effectiveness of these different modules in the proposed algorithm, this subsection conducts ablation experiments by separately removing the low-rank self-representation guidance module ($\gamma = 0$), the sparse constraint ($\beta = 0$), and the structure preservation term ($\lambda = 0$), to verify the roles played by each module. The ablation experiments are conducted using 13 widely used test images (as shown in Figure **??**) and applying these modules to image denoising. The average PSNR results are shown in Table 10. It can be observed that the low-rank self-representation also has the effect of noise removal, and the group sparse representation model guided by low-rank self-representation achieves a significant improvement in denoising performance compared to the single group sparse representation model. Additionally, the introduced structure preservation module in this chapter also contributes to the improvement in performance.

Table 10 Average PSNR (dB) results of image denoising and ablation experiments on 13 commonly used test images

Modules	20	30	40	50	75	100	Average
SR	30.26	27.61	27.27	26.70	24.90	23.72	26.74
LR	25.70	23.23	17.59	15.70	12.30	9.18	17.28
SR+LR	**32.24**	30.13	28.56	27.60	25.66	24.23	28.07
SR+LR+SP	32.20	**30.25**	**28.77**	**27.68**	**25.69**	**24.30**	**28.15**

To further reveal the roles of each module in the proposed algorithm, Figure 13 and 14 respectively demonstrate the denoising results of each module on images *Lena* and *Plants*. As shown

Table 11 Comparison with the method proposed in [71] in the image denoising task

Methods		20	30	40	50	75	100
SRLR	PSNR	32.23	30.24	28.81	27.73	25.72	24.40
	SSIM	0.9046	0.8711	0.8450	0.8198	0.7662	0.7255
LRSR-SP	PSNR	32.20	30.25	28.77	27.68	25.69	24.30
	SSIM	**0.9062**	**0.8764**	**0.8477**	**0.8231**	**0.7687**	**0.7262**

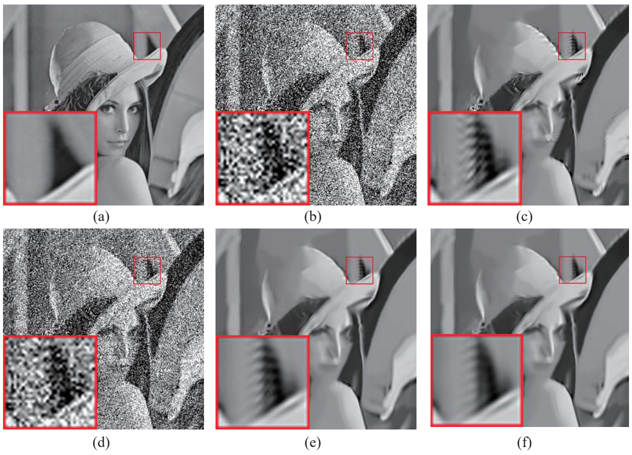

Fig. 13: Visualization of algorithms for denoising image *Lena* under noise $\sigma_E = 75$: (a) Original image, (b) Noisy image, (c) SR (PSNR = 25.04 dB, SSIM = 0.7487), (d) LR (PSNR = 12.31 dB, SSIM = 0.1234), (e) SR+LR (PSNR = 25.50 dB, SSIM = 0.7554), and (f) **SR+LR+SP (PSNR = 25.51 dB, SSIM = 0.7562).**

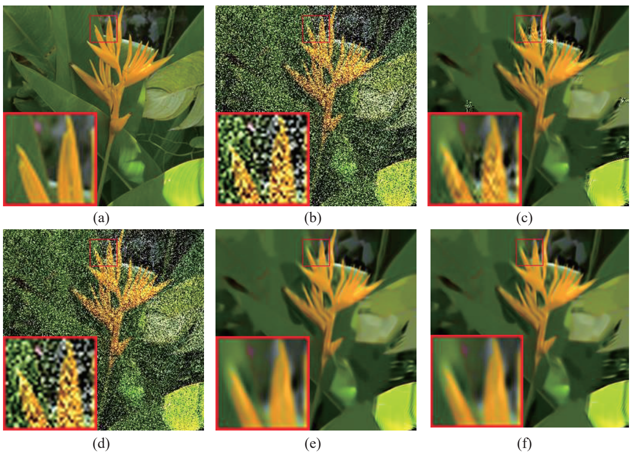

Fig. 14: Visualization of algorithms for denoising image *Plants* under noise $\sigma_E = 75$: (a) Original image, (b) Noisy image, (c) SR (PSNR = 25.51 dB, SSIM = 0.7116), (d) LR (PSNR = 12.32 dB, SSIM = 0.0820), (e) SR+LR (PSNR = 26.46 dB, SSIM = 0.7270), and (f) **SR+LR+SP (PSNR = 26.50 dB, SSIM = 0.7278).**

in Figure 13(c) and Figure 14(c), the sparse representation module indeed serves as an effective tool for image restoration, but it is susceptible to noise, resulting in some undesirable artifacts such as pseudo structures. Although the low-rank self-representation has a minor effect on denoising, combining the sparse representation model with the low-rank self-representation significantly improves the denoising performance, as illustrated in Figure 13(e) and Figure 14(e). Similarly, by introducing the structure preservation module, it can be observed from Figure 13(f) and Figure 14(f) that the images retain well-preserved texture details.

In addition, our previous work[71] also integrated the sparsity and low-rank self-representation properties of images. However, that method was based on sparse coding for self-representation learning, leading to suboptimal solutions because each set of sparse coding coefficients could not guarantee low-rank self-representation properties. In this ablation experiment, we compared the proposed method with the method proposed in our previous work. The PSNR and SSIM results are shown in Table 11. From the table, it can be seen that the proposed algorithm outperforms the previous method in terms of SSIM, which is closer to the human visual system's intuitive evaluation mechanism for image quality. This further demonstrates the effectiveness of the proposed method.

5 Conclusion

Most existing group sparse representation models overlook the similarity relationships between non-local image blocks, while leveraging these relationships can effectively preserve texture information in images. Group sparse representation models apply simple sparsity constraints only to each image block within a group, neglecting other beneficial characteristics of images. To further explore the intrinsic properties of natural images, this chapter proposes a low-rank self-representation guided group sparse representation image restoration algorithm. Specifically, in addition to utilizing the group sparse representation regularization term, this algorithm also utilizes the low-rank self-representation property to jointly estimate the reconstructed image block groups. This low-rank self-representation model can better characterize the intrinsic properties of natural images, namely the correlation between similar image blocks. Additionally, to ensure that the learned sparse representation also preserves the similarity structure between image blocks, the algorithm also performs self-representation learning on the sparse representation, making the self-representation obtained as close as possible to the original self-representation between image blocks. Extensive experimental results demonstrate that this algorithm performs excellently in image restoration tasks such as image denoising and image deblocking.

However, this research still has limitations because it can only achieve excellent performance in scenarios with additive Gaussian noise. In future research, we will consider other noise distributions or multiplicative noise. Furthermore, since the proposed algorithm is self-supervised, it only utilizes the intrinsic information of the degraded images themselves without leveraging external prior knowledge, which limits the improvement of the current algorithm's performance. This is also a challenge that needs to be addressed in future work.

Author contributions

Yaxian Gao: Data curation; Formal analysis; Writingąłoriginal draft. **Zhaoyuan Cai**: Data curation; Formal analysis; Writingąłoriginal draft. **Xianghua Xie**: Conceptualization; Writing-review & editing. **Jingjing Deng**: Conceptualization; Writing-review & editing. **Zengfa Dou**: Resources; Validation. **Xiaoke Ma** (corresponding author): Conceptualization; Funding acquisition; Supervision; Writing-review & editing.

Acknowledgments

This work was supported by the Shaanxi Key Research and Development Program (Program No. 2021ZDLGY02-02).

Conflict of interest statement

The authors do not have any possible conflicts of interest.

Data availability statement

The data that support the findings of this study are available from the corresponding author upon reasonable request.

6 References

1 Banham, M.R., Katsaggelos, A.K.: 'Digital image restoration', *IEEE signal processing magazine*, 1997, **14**, (2), pp. 24–41

2 Elad, M., Aharon, M.: 'Image denoising via sparse and redundant representations over learned dictionaries', *IEEE Transactions on Image processing*, 2006, **15**, (12), pp. 3736–3745

3 Yang, J., Wright, J., Huang, T., Ma, Y. 'Image super-resolution as sparse representation of raw image patches'. In: 2008 IEEE conference on computer vision and pattern recognition. (IEEE, 2008. pp. 1–8

4 Jung, C., Jiao, L., Qi, H., Sun, T.: 'Image deblocking via sparse representation', *Signal Processing: Image Communication*, 2012, **27**, (6), pp. 663–677

5 Rudin, L.I., Osher, S., Fatemi, E.: 'Nonlinear total variation based noise removal algorithms', *Physica D: nonlinear phenomena*, 1992, **60**, (1-4), pp. 259–268

6 Osher, S., Burger, M., Goldfarb, D., Xu, J., Yin, W.: 'An iterative regularization method for total variation-based image restoration', *Multiscale Modeling & Simulation*, 2005, **4**, (2), pp. 460–489

7 Bappy, D., Jeon, I.: 'Combination of hybrid median filter and total variation minimisation for medical x-ray image restoration', *IET Image Processing*, 2016, **10**, (4), pp. 261–271

8 Dong, W., Zhang, L., Shi, G., Li, X.: 'Nonlocally centralized sparse representation for image restoration', *IEEE transactions on Image Processing*, 2012, **22**, (4), pp. 1620–1630

9 Ji, H., Huang, S., Shen, Z., Xu, Y.: 'Robust video restoration by joint sparse and low rank matrix approximation', *SIAM Journal on Imaging Sciences*, 2011, **4**, (4), pp. 1122–1142

10 Dong, W., Shi, G., Li, X.: 'Nonlocal image restoration with bilateral variance estimation: a low-rank approach', *IEEE transactions on image processing*, 2012, **22**, (2), pp. 700–711

11 Gu, S., Zhang, L., Zuo, W., Feng, X. 'Weighted nuclear norm minimization with application to image denoising'. In: Proceedings of the IEEE conference on computer vision and pattern recognition. (, 2014. pp. 2862–2869

12 Liu, D., Wen, B., Fan, Y., Loy, C.C., Huang, T.S.: 'Non-local recurrent network for image restoration', *Advances in neural information processing systems*, 2018, **31**

13 Mastan, I.D., Raman, S. 'Deepcfl: Deep contextual features learning from a single image'. In: Proceedings of the IEEE/CVF Winter Conference on Applications of Computer Vision. (, 2021. pp. 2897–2906

14 Zha, Z., Yuan, X., Zhou, J.T., Zhou, J., Wen, B., Zhu, C. 'The power of triply complementary priors for image compressive sensing'. In: 2020 IEEE International Conference on Image Processing (ICIP). (IEEE, 2020. pp. 983–987

15 Mataev, G., Milanfar, P., Elad, M. 'Deepred: Deep image prior powered by red'. In: Proceedings of the IEEE/CVF International Conference on Computer Vision Workshops. (, 2019. pp. 0–0

16 Zamir, S.W., Arora, A., Khan, S., Hayat, M., Khan, F.S., Yang, M.H. 'Restormer: Efficient transformer for high-resolution image restoration'. In: Proceedings of the IEEE/CVF conference on computer vision and pattern recognition. (, 2022. pp. 5728–5739

17 Shen, L., Pauly, J., Xing, L.: 'Nerp: implicit neural representation learning with prior embedding for sparsely sampled image reconstruction', *IEEE Transactions on Neural Networks and Learning Systems*, 2022,

18 Chen, L., Chu, X., Zhang, X., Sun, J. 'Simple baselines for image restoration'. In: European Conference on Computer Vision. (Springer, 2022. pp. 17–33

19 Zha, Z., Wen, B., Yuan, X., Zhou, J., Zhu, C. 'Simultaneous nonlocal low-rank and deep priors for poisson denoising'. In: ICASSP 2022-2022 IEEE International Conference on Acoustics, Speech and Signal Processing (ICASSP). (IEEE, 2022. pp. 2320–2324

20 Wu, W., Chen, M., Xiang, Y., Zhang, Y., Yang, Y.: 'Recent progress in image denoising: A training strategy perspective', *IET Image Processing*, 2023,

21 Deeba, F., Kun, S., Ali.Dharejo, F., Zhou, Y.: 'Sparse representation based computed tomography images reconstruction by coupled dictionary learning algorithm', *IET image Processing*, 2020, **14**, (11), pp. 2365–2375

22 Zha, Z., Yuan, X., Wen, B., Zhang, J., Zhu, C.: 'Nonconvex structural sparsity residual constraint for image restoration', *IEEE Transactions on Cybernetics*, 2021,

23 Yuan, W., Liu, H., Liang, L.: 'Image restoration via exponential scale mixture-based simultaneous sparse prior', *IET Image Processing*, 2022, **16**, (12), pp. 3268–3283

24 Xu, W., Zhu, Q., Qi, N., Chen, D.: 'Deep sparse representation based image restoration with denoising prior', *IEEE Transactions on Circuits and Systems for Video Technology*, 2022, **32**, (10), pp. 6530–6542

25 Buades, A., Coll, B., Morel, J.M. 'A non-local algorithm for image denoising'. In: 2005 IEEE computer society conference on computer vision and pattern recognition (CVPR'05). vol. 2. (Ieee, 2005. pp. 60–65

26 Dabov, K., Foi, A., Katkovnik, V., Egiazarian, K.: 'Image denoising by sparse 3-d transform-domain collaborative filtering', *IEEE Transactions on image processing*, 2007, **16**, (8), pp. 2080–2095

27 Zhang, J., Zhao, D., Gao, W.: 'Group-based sparse representation for image restoration', *IEEE transactions on image processing*, 2014, **23**, (8), pp. 3336–3351

28 Li, X., Shen, H., Li, H., Zhang, L.: 'Patch matching-based multitemporal group sparse representation for the missing information reconstruction of remote-sensing images', *IEEE Journal of Selected Topics in Applied Earth Observations and Remote Sensing*, 2016, **9**, (8), pp. 3629–3641

29 Wang, Q., Zhang, X., Wu, Y., Tang, L., Zha, Z.: 'Nonconvex weighted ℓ_p minimization based group sparse representation framework for image denoising', *IEEE Signal Processing Letters*, 2017, **24**, (11), pp. 1686–1690

30 Aharon, M., Elad, M., Bruckstein, A.: 'K-svd: An algorithm for designing overcomplete dictionaries for sparse representation', *IEEE Transactions on signal processing*, 2006, **54**, (11), pp. 4311–4322

31 Daubechies, I.: 'The wavelet transform, time-frequency localization and signal analysis', *IEEE transactions on information theory*, 1990, **36**, (5), pp. 961–1005

32 Mairal, J., Bach, F., Ponce, J., Sapiro, G., Zisserman, A. 'Non-local sparse models for image restoration'. In: 2009 IEEE 12th international conference on computer vision. (IEEE, 2009. pp. 2272–2279

33 Zhang, J., Zhang, Y., Gu, J., Zhang, Y., Kong, L., Yuan, X.: 'Accurate image restoration with attention retractable transformer', *ArXiv*, 2022, **abs/2210.01427**. Available from: `https://api.semanticscholar.org/CorpusID:252693111`

34 Chen, X., Li, H., Li, M., Pan, J. 'Learning a sparse transformer network for effective image deraining'. In: Proceedings of the IEEE/CVF Conference on Computer Vision and Pattern Recognition. (, 2023. pp. 5896–5905

35 Zhou, S., Chen, D., Pan, J., Shi, J., Yang, J. 'Adapt or perish: Adaptive sparse transformer with attentive feature refinement for image restoration'. In: Proceedings of the IEEE/CVF Conference on Computer Vision and Pattern Recognition. (, 2024. pp. 2952–2963

36 Xu, J., Zhang, L., Zuo, W., Zhang, D., Feng, X. 'Patch group based nonlocal self-similarity prior learning for image denoising'. In: Proceedings of the IEEE international conference on computer vision. (, 2015. pp. 244–252

37 Zha, Z., Wen, B., Yuan, X., Zhou, J., Zhu, C., Kot, A.C.: 'A hybrid structural sparsification error model for image restoration', *IEEE Transactions on Neural Networks and Learning Systems*, 2021, **33**, (9), pp. 4451–4465

38 Yuan, W., Liu, H., Liang, L.: 'Joint group dictionary-based structural sparse representation for image restoration', *Digital Signal Processing*, 2023, **137**, pp. 104029

39 Zha, Z., Wen, B., Yuan, X., Zhou, J., Zhu, C., Kot, A.C.: 'Low-rankness guided group sparse representation for image restoration', *IEEE Transactions on Neural Networks and Learning Systems*, 2022,

40 Niknejad, M., Rabbani, H., Babaie.Zadeh, M.: 'Image restoration using gaussian mixture models with spatially constrained patch clustering', *IEEE Transactions on Image Processing*, 2015, **24**, (11), pp. 3624–3636

41 Candes, E.J., Tao, T.: 'Near-optimal signal recovery from random projections: Universal encoding strategies?', *IEEE transactions on information theory*, 2006, **52**, (12), pp. 5406–5425

42 Donoho, D.L.: 'For most large underdetermined systems of linear equations the minimal ℓ_1-norm solution is also the sparsest solution', *Communications on Pure and Applied Mathematics: A Journal Issued by the Courant Institute of Mathematical Sciences*, 2006, **59**, (6), pp. 797–829

43 Chartrand, R., Yin, W. 'Iteratively reweighted algorithms for compressive sensing'. In: 2008 IEEE international conference on acoustics, speech and signal processing. (IEEE, 2008. pp. 3869–3872

44 Mazumder, R., Friedman, J.H., Hastie, T.: 'Sparsenet: Coordinate descent with nonconvex penalties', *Journal of the American Statistical Association*, 2011, **106**, (495), pp. 1125–1138

45 Vidal, R., Favaro, P.: 'Low rank subspace clustering (lrsc)', *Pattern Recognition Letters*, 2014, **43**, pp. 47–61

46 Zuo, W., Meng, D., Zhang, L., Feng, X., Zhang, D. 'A generalized iterated shrinkage algorithm for non-convex sparse coding'. In: Proceedings of the IEEE international conference on computer vision. (, 2013. pp. 217–224

47 Krishnan, D., Fergus, R.: 'Fast image deconvolution using hyper-laplacian priors', *Advances in neural information processing systems*, 2009, **22**

48 Zhang, K., Zuo, W., Chen, Y., Meng, D., Zhang, L.: 'Beyond a gaussian denoiser: Residual learning of deep cnn for image denoising', *IEEE transactions on image processing*, 2017, **26**, (7), pp. 3142–3155

49 Plotz, T., Roth, S. 'Benchmarking denoising algorithms with real photographs'. In: Proceedings of the IEEE conference on computer vision and pattern recognition. (, 2017. pp. 1586–1595

50 Sheikh, H.: 'Live image quality assessment database release 2', *http://live ece utexas edu/research/quality*, 2005,

51 Zeyde, R., Elad, M., Protter, M. 'On single image scale-up using sparse-representations'. In: International conference on curves and surfaces. (Springer, 2010. pp. 711–730

52 Zoran, D., Weiss, Y. 'From learning models of natural image patches to whole image restoration'. In: 2011 international conference on computer vision. (IEEE, 2011. pp. 479–486

53 Zhang, L., Dong, W., Zhang, D., Shi, G.: 'Two-stage image denoising by principal component analysis with local pixel grouping', *Pattern recognition*, 2010, **43**, (4), pp. 1531–1549

54 Luo, E., Chan, S.H., Nguyen, T.Q.: 'Adaptive image denoising by mixture adaptation', *IEEE transactions on image processing*, 2016, **25**, (10), pp. 4489–4503

55 Liu, H., Tan, S.: 'Image regularizations based on the sparsity of corner points', *IEEE Transactions on Image Processing*, 2018, **28**, (1), pp. 72–87

56 Zha, Z., Yuan, X., Zhou, J., Zhu, C., Wen, B.: 'Image restoration via simultaneous nonlocal self-similarity priors', *IEEE Transactions on Image Processing*, 2020, **29**, pp. 8561–8576

57 Zha, Z., Yuan, X., Wen, B., Zhang, J., Zhou, J., Zhu, C.: 'Image restoration using joint patch-group-based sparse representation', *IEEE Transactions on Image Processing*, 2020, **29**, pp. 7735–7750

58 Chen, Y., Pock, T.: 'Trainable nonlinear reaction diffusion: A flexible framework for fast and effective image restoration', *IEEE transactions on pattern analysis and machine intelligence*, 2016, **39**, (6), pp. 1256–1272

59 Quan, Y., Chen, M., Pang, T., Ji, H. 'Self2self with dropout: Learning self-supervised denoising from single image'. In: Proceedings of the IEEE/CVF conference on computer vision and pattern recognition. (, 2020. pp. 1890–1898

60 Foi, A., Katkovnik, V., Egiazarian, K.: 'Pointwise shape-adaptive dct for high-quality denoising and deblocking of grayscale and color images', *IEEE transactions on image processing*, 2007, **16**, (5), pp. 1395–1411

61 Ren, J., Liu, J., Li, M., Bai, W., Guo, Z. 'Image blocking artifacts reduction via patch clustering and low-rank minimization'. In: 2013 Data Compression Conference. (IEEE, 2013. pp. 516–516

62 Gu, S., Xie, Q., Meng, D., Zuo, W., Feng, X., Zhang, L.: 'Weighted nuclear norm minimization and its applications to low level vision', *International journal of computer vision*, 2017, **121**, (2), pp. 183–208
63 Zhang, X., Xiong, R., Fan, X., Ma, S., Gao, W.: 'Compression artifact reduction by overlapped-block transform coefficient estimation with block similarity', *IEEE transactions on image processing*, 2013, **22**, (12), pp. 4613–4626
64 Zhao, C., Zhang, J., Ma, S., Fan, X., Zhang, Y., Gao, W.: 'Reducing image compression artifacts by structural sparse representation and quantization constraint prior', *IEEE Transactions on Circuits and Systems for Video Technology*, 2016, **27**, (10), pp. 2057–2071
65 Young, S.I., Naman, A.T., Taubman, D.: 'Cogl: Coefficient graph laplacians for optimized jpeg image decoding', *IEEE Transactions on Image Processing*, 2018, **28**, (1), pp. 343–355
66 Dong, C., Deng, Y., Loy, C.C., Tang, X. 'Compression artifacts reduction by a deep convolutional network'. In: Proceedings of the IEEE international conference on computer vision. (, 2015. pp. 576–584
67 Fu, X., Zha, Z.J., Wu, F., Ding, X., Paisley, J. 'Jpeg artifacts reduction via deep convolutional sparse coding'. In: Proceedings of the IEEE/CVF International Conference on Computer Vision. (, 2019. pp. 2501–2510
68 Fu, X., Wang, M., Cao, X., Ding, X., Zha, Z.J.: 'A model-driven deep unfolding method for jpeg artifacts removal', *IEEE Transactions on Neural Networks and Learning Systems*, 2021,
69 Wang, Z., Bovik, A.C., Sheikh, H.R., Simoncelli, E.P.: 'Image quality assessment: from error visibility to structural similarity', *IEEE transactions on image processing*, 2004, **13**, (4), pp. 600–612
70 Immerkaer, J.: 'Fast noise variance estimation', *Computer vision and image understanding*, 1996, **64**, (2), pp. 300–302
71 Cai, Z., Xie, X., Deng, J., Dou, Z., Tong, B., Ma, X.: 'Image restoration with group sparse representation and low-rank group residual learning', *IET Image Processing*, 2024, **18**, (3), pp. 741–760

Table 3 Average PSNR(dB) results of image denoising compared with classical methods on DND dataset

Applied	Evaluated	BM3D	LSSC	EPLL	LPCA	NCSR	aGMM	NLN-CDR	SNSS	**Ours**
RAW	RAW	46.52	45.04	46.32	46.22	42.04	45.58	42.47	43.58	**46.63**
RAW	sRGB	37.91	37.11	37.37	36.55	36.28	36.02	36.23	35.99	**37.99**
RAW+VST	RAW	**47.05**	46.98	46.85	46.72	45.58	45.09	45.39	44.98	47.01
RAW+VST	sRGB	36.78	36.85	35.89	36.56	36.12	36.84	36.28	36.44	**36.91**

Table 4 Average SSIM results of image denoising compared with classical methods on DND dataset

Applied	Evaluated	BM3D	LSSC	EPLL	LPCA	NCSR	aGMM	NLN-CDR	SNSS	**Ours**
RAW	RAW	0.9701	0.9655	0.9583	0.958	0.9537	0.962	0.9674	0.9532	**0.9724**
RAW	sRGB	0.9218	0.919	0.9012	0.9242	0.9273	0.9242	0.9101	0.9154	**0.9313**
RAW+VST	RAW	**0.9542**	0.9172	0.9143	0.9111	0.9204	0.9044	0.9174	0.9077	0.9502
RAW+VST	sRGB	0.9135	0.8995	0.9045	0.9235	0.9005	0.9141	0.9006	0.9133	**0.9258**

Table 6 Average PSNR (dB) results of image deblocking compared with the classic method on the datasets LIVE1 and Classic5 (image size: 256×256)

LIVE1 dataset (image size: 256×256)											
Q	**JPEG**	**BM3D**	**SA-DCT**	**PC-LRM**	**ANCE**	**WNNM**	**SSR-QC**	**COGL**	**JPG-SR**	**NSSRC**	**Ours**
10	26.37	27.16	27.23	27.24	27.24	27.25	27.26	27.38	27.29	27.43	**27.45**
20	28.55	29.21	29.24	29.28	29.29	29.29	29.33	29.46	29.37	29.53	**29.55**
30	29.86	30.45	30.48	30.54	30.57	30.55	30.60	30.74	30.75	30.85	**30.86**
40	30.80	31.35	31.37	31.45	31.51	31.46	31.57	31.66	31.71	**31.82**	31.81
Average	28.90	29.54	29.58	29.63	29.65	29.64	29.69	29.81	29.78	29.91	**29.92**
Classic5 dataset (image size: 256×256)											
Q	**JPEG**	**BM3D**	**SA-DCT**	**PC-LRM**	**ANCE**	**WNNM**	**SSR-QC**	**COGL**	**JPG-SR**	**NSSRC**	**Ours**
10	27.57	28.69	28.72	28.79	28.77	28.78	28.83	28.93	28.78	28.97	**29.03**
20	29.90	30.87	30.89	30.98	30.96	30.98	31.07	31.13	31.12	31.23	**31.26**
30	31.21	32.07	32.09	32.21	32.22	32.21	32.34	32.39	32.50	**32.55**	32.54
40	32.14	32.94	32.96	33.09	33.16	33.10	33.30	33.29	33.46	**33.54**	33.51
Average	30.21	31.14	31.17	31.27	31.28	31.27	31.39	31.43	31.47	31.57	**31.59**

Table 7 Average SSIM results of image deblocking compared with the classic method on the datasets LIVE1 and Classic5 (image size: 256×256)

LIVE1 dataset (image size: 256×256))											
Q	**JPEG**	**BM3D**	**SA-DCT**	**PC-LRM**	**ANCE**	**WNNM**	**SSR-QC**	**COGL**	**JPG-SR**	**NSSRC**	**Ours**
10	0.7611	0.7877	0.7869	0.7835	0.7879	0.7824	0.7859	0.7957	0.7931	0.7956	**0.7971**
20	0.8423	0.8591	0.8571	0.8550	0.8585	0.8542	0.8576	0.8642	0.8630	0.8645	**0.8651**
30	0.8791	0.8917	0.8903	0.8892	0.8913	0.8888	0.8913	0.8952	0.8967	0.8963	**0.8970**
40	0.8998	0.9103	0.9093	0.9089	0.9102	0.9087	0.9099	0.9129	0.9145	0.9148	**0.9144**
Average	0.8456	0.8622	0.8609	0.8592	0.8620	0.8585	0.8612	0.8670	0.8668	0.8678	**0.8684**
Classic5 dataset (image size: 256×256))											
Q	**JPEG**	**BM3D**	**SA-DCT**	**PC-LRM**	**ANCE**	**WNNM**	**SSR-QC**	**COGL**	**JPG-SR**	**NSSRC**	**Ours**
10	0.7715	0.8087	0.8060	0.8043	0.8081	0.8033	0.8094	0.8134	0.8134	0.8168	**0.8195**
20	0.8519	0.8753	0.8728	0.8723	0.8730	0.8714	0.8740	0.8751	0.8796	0.8802	**0.8807**
30	0.8844	0.9018	0.9002	0.9003	0.9002	0.8998	0.9017	0.9012	0.9063	0.9060	**0.9061**
40	0.9036	0.9178	0.9168	0.9170	0.9172	0.9167	0.9180	0.9175	0.9225	**0.9226**	0.9217
Average	0.8529	0.8759	0.8740	0.8735	0.8746	0.8728	0.8758	0.8768	0.8805	0.8814	**0.8820**